Environmental Science Nano

ROYAL SOCIETY OF CHEMISTRY

PAPER

View Article Online
View Journal | View Issue

Cite this: *Environ. Sci.: Nano*, 2023, 10, 824

A single-cell based mass cytometry study on heterogeneous interactions between upconversion nanoparticles and human immune cells†

Zayakhuu Gerelkhuu,[ab] Haribalan Perumalsamy,[ab] Mahnaz Maddahfar,[c] Dayong Jin,[cd] Jaewoo Song[e] and Tae Hyun Yoon *[abf]

To encourage the use of lanthanide-doped upconversion nanoparticles (UCNPs) in a wide range of biomedical applications, it is necessary to perform comprehensive assessments of their toxicity. In particular, the cellular association and their heterogeneous interactions with human immune cells must be clarified prior to their use as a diagnostic or therapeutic tool in biomedical applications. Recent advancements of high-throughput single-cell technologies enabled us to characterize the complex interactions between nanoparticles and human immune cells and allowed us to gain a better understanding of their heterogeneous nature. In this study, using a single-cell based mass cytometry technique, we investigated the heterogeneous interactions of Yb^{3+}/Er^{3+}-doped $NaYF_4$ UCNPs with human peripheral blood mononuclear cells (hPBMCs). Based on the manual gating strategy applied to the signals of 14 metal isotope labelled surface markers, twelve immune cell types, such as classical/intermediate/non-classical monocytes, naïve/memory B cells, plasmacytoid/myeloid dendritic cells, naïve/memory T helper and T killer cells, and neutrophils were identified from hPBMCs. The relative levels of cell-associated UCNPs and cell death were estimated based on the measurements of ^{89}Y intensity and cisplatin uptake, respectively. Among various immune cell types, the phagocytic cells, such as monocytes and dendritic cells, displayed greater affinity to the UCNPs than the other non-phagocytic cells. Additionally, we utilized automated and unsupervised clustering algorithm, such as phenograph (PG), to profile additional subsets of these phagocytic cells, such as PG#1, 4, 18 of the classical monocytes and PG#2, 3, 19, 27 of the myeloid dendritic cells. This single-cell based mass cytometry study on UCNPs and hPBMCs demonstrated a new innovative approach to understand heterogeneous interactions of conventional nanomaterials with complex human immune systems, which will facilitate the safe implementation of nanomaterials in biomedical applications.

Received 5th September 2022,
Accepted 6th February 2023

DOI: 10.1039/d2en00821a

rsc.li/es-nano

Environmental significance

Lanthanide-based and polymer-coated upconversion nanoparticles (UCNPs) have shown great potential for environmental and biological applications such as the photodegradation of organic contaminants, biosensors, and photodynamic therapy. Here, we used single-cell based mass cytometry approach to investigate the heterogeneous interactions of POEGMEA-*b*-PMAEP polymer-coated $NaYF_4$:Yb^{3+}/Er^{3+} UCNPs in human primary immune cells. Our findings suggest that NP uptake and toxicity in immune cells vary greatly, not only between cell types but also within the same cell type. Additionally, phenograph clustering was used for the identification of sub-clusters of major immune cell types and their specific surface marker expression. This study demonstrates that single-cell based mass cytometry can open up new avenues for future research into the interactions of lanthanide-based NPs with living systems and the environment.

[a] *Department of Chemistry, College of Natural Sciences, Hanyang University, Seoul 04763, Republic of Korea. E-mail: taeyoon@hanyang.ac.kr*
[b] *Institute of Next Generation Material Design, Hanyang University, Seoul 04763, Republic of Korea*
[c] *Institute for Biomedical Materials and Devices (IBMD), School of Mathematics and Physical Sciences, Faculty of Science, University of Technology Sydney, Sydney, New South Wales 2007, Australia*
[d] *UTS-SUStech Joint Research Centre for Biomedical Materials and Devices, Department of Biomedical Engineering, Southern University of Science and Technology, Shenzhen, Guangdong 518055, P.R. China*
[e] *Department of Laboratory Medicine, College of Medicine, Yonsei University, Seoul 03722, Republic of Korea*
[f] *Center for Next Generation Cytometry, Hanyang University, Seoul 04763, Republic of Korea*

† Electronic supplementary information (ESI) available. See DOI: https://doi.org/10.1039/d2en00821a

Introduction

Nanotechnology brings exciting new opportunities and features for their biomedical applications including cancer theragnostics,[1] nanomedicine,[2] bioimaging,[3] and biosensors.[4–6] Inorganic nanoparticles (NPs) can be easily functionalized to improve the stability, biocompatibility, biodistribution, and target specific characteristics.[7] Among these, fluorescence inorganic nanomaterials are mostly used in imaging, photodynamic therapy (PDT),[8] and sensors,[9] such as quantum dots (QDs), carbon dots (CDs),[10] heavy metal-based NPs, and organic polymers.[11,12] For example, gadolinium, platinum, and bismuth-based NPs are being developed as contrast agents for X-ray and magnetic resonance imaging (MRI).[13–16] However, conventional nanomaterials can be triggered by ultraviolet (UV) light. They have several disadvantages including very limited light penetration depth, cell auto-fluorescence, and photobleaching. Inversely, lanthanide-doped upconversion nanoparticles (UCNPs) convert low-energy light into higher-energy light by multiphoton absorption, which is advantageous to increasing the penetration depth and reducing autofluorescence and photobleaching under a near-infrared (NIR) laser.[17,18] The unique optical properties of UCNPs make them the best candidates for effective biomedical applications, such as MRI,[19] chemical sensing,[4] drug delivery,[20] color display technologies,[21] solar cells,[22] and photoswitching.[23] With the increasing application of UCNPs, there are increasing concerns about the possible toxicity of UCNPs to human health.[24] Researchers have demonstrated that in acidic circumstances, UCNPs may produce lanthanide ions, which are likely to interact with phosphate-containing biomolecules in living organisms, and ultimately trigger cell autophagy and death.[25,26] Therefore, it is important to assess UCNPs toxicity and identify the cellular response in human immune cells to apply UCNPs in clinical and biological research approaches.

Numerous research studies on the cytotoxicity of UCNPs have been conducted, including observation of the cellular morphology, identification of biologically important proteins and enzymes, and the evaluation of DNA damage before and after exposure. Previous cytotoxicity investigations of UCNPs were typically carried out using simple assays, such as MTT and MTS assays *in vitro* at the cellular level.[27–29] Moreover, the data obtained from the evaluation of homogenous single-cell types are insufficient, and may even cause misconceptions of the NPs toxicity assessment. To address this, extensive toxicity assessments in heterogeneous cell types may contribute to more complete knowledge of the UCNPs cytotoxicity and nano-safety assessment. However, there are challenges to profiling at the single-cell level, owing to the insufficient implementation of high-throughput and deep phenotyping technologies that are required. Fluorescence-based flow cytometry and single-cell inductively coupled plasma mass spectrometry (sc-ICP-MS) have been primarily used to address single-cell behavior. However, the overlapping flow cytometry signals of the fluorophore-conjugated markers and the limited detection channel of sc-ICP-MS may lead to mistakes in the analysis.[30] To overcome those issues, a technique that uses mass spectrometry to improve the precision of flow cytometry analysis was recently created. The combination of the two techniques, known as cytometry by time of flight (CyTOF), enables the measurement of more than 40 cellular parameters as channels at single-cell resolution. Despite the fluorescence-based cytometry, CyTOF uses metal isotope tagged probes to discriminate elements based on their mass/charge ratio (m/z), with minimal overlap and background cellular signal. All of these attributes simplify the large panel experimental design, allowing for high-dimensional cytometry studies that would not be possible otherwise. Additionally, the complexity of the immune system is designed to protect against various foreign substances, pathogens, or tumors, which cause various autoimmune disorders and allergies, leading to immune dysfunction.[31,32] Thus, it is necessary to reveal the complexity of the cellular interactions and various biological reactions caused by UCNPs in the human immune system at the single-cell level.

In this work, we performed a comprehensive approach to study complex interactions between heterogeneous immune cells (from human peripheral blood mononuclear cells (hPBMC)) and UCNPs at the single-cell level. Single-cell mass cytometry analysis was conducted to reveal the heterogeneity of the immunological response towards the dose-dependent polymer-coated lanthanide-doped upconversion nanoparticles (UCNP@POEGMEA-*b*-PMEAP is denoted as UCNP@polymer) in hPBMC. Furthermore, significant heterogeneous immune cell types (including neutrophils, monocytes, dendritic cells, B cells, and T cells) and their subsets' population differences were identified from hPBMC by 14 different surface markers. For high dimensional data visualization, dimensionality reduction and automated clustering tools (such as uniform manifold approximation and projection (UMAP) and phenograph (PG)) were used to identify new characteristics of the immunological changes from untreated and treated samples. The cell subsets identification from significant immune cell types were comprehensively visualized by performing the PG clustering algorithm.

Experimental section

Synthesis and functionalization of the lanthanide-doped upconversion nanoparticles

In this study, polymer-coated $NaYF_4$:Yb^{3+}/Er^{3+} upconversion nanoparticles (UCNP@POEGMEA-*b*-PMEAP) were provided by the Jin group from University of Technology Sydney (UTS), Australia, and the synthesis and functionalization procedures have been previously reported.[33,34] Briefly, $YCl_3{\cdot}6H_2O$ (0.78 mmol), $YbCl_3{\cdot}6H_2O$ (0.20 mmol), and $ErCl_3{\cdot}6H_2O$ (0.02 mmol) were added to a 50 mL flask containing 6 mL of oleic acid (OA) and 15 mL of 1-octadecene (ODE). The mixture was heated to 160 °C for 30 min, and then cooled to room

temperature. A solution of 4 mmol of NH_4F and 2.5 mmol of NaOH in 5 mL of methanol was added, and then the solution was kept at room temperature for 30 min. The mixture was then heated to 120 °C under argon for 20 min to remove methanol and water. The solution was finally heated to 300 °C under an argon atmosphere for 1.5 h, and then cooled to room temperature. The nanocrystals were precipitated with 10 mL of ethanol, collected by centrifugation. The product was washed with cyclohexane, ethanol and methanol four times, and the final $NaYF_4$:Yb^{3+}/Er^{3+} nanocrystals were re-dispersed in 10 mL cyclohexane for further use.

OA-capped UCNPs are required to be transferred from the oil phase to aqueous phase for bio-medical applications. To this end, the diblock copolymer (POEGMEA-*b*-PMAEP) composed of oligo ethylene glycol methyl ether acrylate (OEGMEA) and block-bearing phosphate group (MAEP) prepared by reversible addition fragmentation chain transfer (RAFT) polymerization, was used as a hydrophilic ligand to make the nanoparticles biocompatible *via* a ligand exchange process.[33] In a common modification method, 10 mg of the polymer with 13 repeating OEGMEA units dissolved in (1 mL) THF (10 mg mL^{-1}), was mixed with 10 mg UCNPs suspended in (1 mL) THF (10 mg mL^{-1}) with the ratio of 1 : 1 in mass. The reaction solution was wrapped tightly *via* parafilm and placed on a gentle shaker for 17 h at room temperature. The polymer-coated UCNPs were then centrifuged at 20 240 × *g* for 30 min, the supernatant was removed, and the UCNPs were washed by resuspension in 1 mL of 3 : 1 THF : Milli-Q water. The wash was repeated 4 times with decreasing concentrations of THF in Milli-Q water, with the last wash performed in 100% water. The well-dispersed UCNPs (abbreviated as UCNP@polymer) were then resuspended in 1 mL Milli-Q water to generate a clear suspension for further use.

Characterization of upconversion nanoparticles

The actual size and morphology of UCNP@OA and UCNP@polymer were characterized using a FEI Tecnai G2 20 transmission electron microscope (TEM) with a beam voltage of 200 kV. TEM samples were prepared at a concentration of 1 mg mL^{-1} and drop-casted onto carbon-coated and glow-discharged TEM grids for UCNP@OA and UCNP@polymer. ATR-FTIR spectra of the dried samples were collected using a Nicolet 7650 system using diffuse reflectance sampling accessories at regular time intervals in the MIR region of 4000–500 cm^{-1} at a resolution of 4 cm^{-1} (64 scans), and analysed using Omnic software. The hydrodynamic size distribution and surface charge of UCNP@polymer were measured for the samples in a disposable cuvette at a concentration of 1 mg mL^{-1}, using a Malvern Instruments Zetasizer Nano ZS instrument equipped with a 4 mV He–Ne laser operating at λ = 633 nm with the high quantum efficiency of the avalanche photodiode detector.

Peripheral blood mononuclear cells isolation

EDTA whole blood was drawn from healthy adult donors with written consent. The study, including volunteer recruitment and blood sample collection, was approved by the Institutional Review Board (IRB) of the College of Medicine, Yonsei University, Seoul, Republic of Korea. Human peripheral blood mononuclear cells (hPBMCs) were isolated by density gradient centrifugation using Ficoll-Paque (GE Healthcare Bio-Sciences, Sweden).

Immunophenotypic characterization of UCNP@polymer treated hPBMC by single-cell mass cytometry

The hPBMCs were treated with UCNP@polymer in RPMI complete media at 0.5, 1, and 2 ppm for 3 h, and incubated at 37 °C under 5% CO_2. Consequently, approximately 2–3 million hPBMCs were stained with 14 surface markers (listed in Table 1.) for single-cell mass cytometry analyses. Briefly, the UCNP@polymer-treated hPBMC were washed with DPBS to remove the excess NPs, then stained with 1.25 μM cisplatin in DPBS for 1 min at room temperature, and quenched with cell staining buffer (CSB). Cells were incubated for 30 min at room temperature with a 50 μL cocktail of metal isotope conjugated antibodies targeting the surface antigens. All antibodies listed in Table 1, with the metal isotope tagged antibodies from Fluidigm, CD3 and HLA-DR antibodies, were conjugated with Maxpar X8 labeling reagent kits (Fluidigm) according to the manufacturer's instructions. Following the wash with CSB, cells were fixed with 1.6% paraformaldehyde (PFA) at room temperature for 20 min, then DNA intercalator (0.125 μM iridium – 191/193; Fluidigm) staining was performed at 4 °C overnight. After multiple washes with CSB, cells (1×10^6 cells per mL) were re-suspended in cell acquisition solution (CAS) with EQ beads (Fluidigm) diluted to a factor of 1 in 10. Cells were acquired at a rate of 200–400 cells per s using a CyTOF 3 Helios mass cytometer (Fluidigm, Corp. USA). Cells were normalized for the signal intensity of EQ beads using Helios software. Cytobank and FlowJo software were used to be the gate populations of interest and

Table 1 Mass cytometry antibody panel

Metal	Target	Clone	Manufacturer
143Nd	CD3	UCHT1	Biolegend
145Nd	CD4	RPA-T4	Fluidigm
146Nd	CD8a	RPA-T8	Fluidigm
159Tb	CD11c	Bu15	Fluidigm
175Lu	CD14	M5E2	Fluidigm
148Nd	CD16	3G8	Fluidigm
142Nd	CD19	HIB19	Fluidigm
147Sm	CD20	2H7	Fluidigm
154Sm	CD45	HI30	Fluidigm
169Tm	CD45RA	HI100	Fluidigm
165Ho	CD61	VI-PL2	Fluidigm
149Sm	CD66a	CD66a-B1.1	Fluidigm
151Eu	CD123	6H6	Fluidigm
152Sm	HLA-DR	L243	Biolegend

export the mean signal intensity for markers across populations and study participants.

Data acquisition and gating strategy

A CyTOF 3 Helios mass cytometer (Fluidigm Corp., USA) was used for data acquisition. The instrument was tuned by optimizing the nebulizer, makeup gas, current, and detector voltage according to the manufacturer's guidelines. To acquire data on the hPBMC samples, the instrument was set to "event mode". The injection speed was kept at 5×10^{-7} L s^{-1}. The push length was set at 13 μs by default.

Cytobank v9.0 (Cytobank, Inc., USA) and FlowJo v10.8.1 (FlowJo, LLC, Ashland, Oregon, OR, USA) were used for data manual gating, visualization, and automated clustering algorithms. Inverse hyperbolic sine (arcsinh) transformation was applied to the raw data. The cell populations were identified by gating based on the surface markers (Table 1). The manual gating strategy is presented in Fig. S1.†

The UMAP dimensionality reduction method was used to visualize single-cell resolution of the data, while automated clustering method was used, such as phenograph. The bivariate plots between the cellular responses and UCNP@polymer association were used to analyse the dose–response relationship and the UCNPs toxicity at a single-cell level.

Limit of detection analysis

To assess the detection limit of UCNP@polymer per cell on the Helios mass cytometry instrument, hPBMCs were treated with UCNP@polymer at 5, 20, 50, 500, 1000, 1500, 2000, 2500, and 3000 ppb for 3 h at 37 °C in RPMI complete media. hPBMCs were stained with cisplatin and the main surface markers for T cells, such as CD45 (154Sm), CD3 (143Nd), CD4 (145Nd), and CD8 (146Nd), according to Fluidigm's protocols. The cells were washed with DPBS twice prior to fixation and Ir cell-ID DNA stains. Cells were resuspended at 1 million per ml in 1:10 calibration EQ beads in Maxpar CAS, and were analysed by Helios mass cytometry. Events that were double positive for the 193Ir and 195Ir DNA stains were gated, and singlets

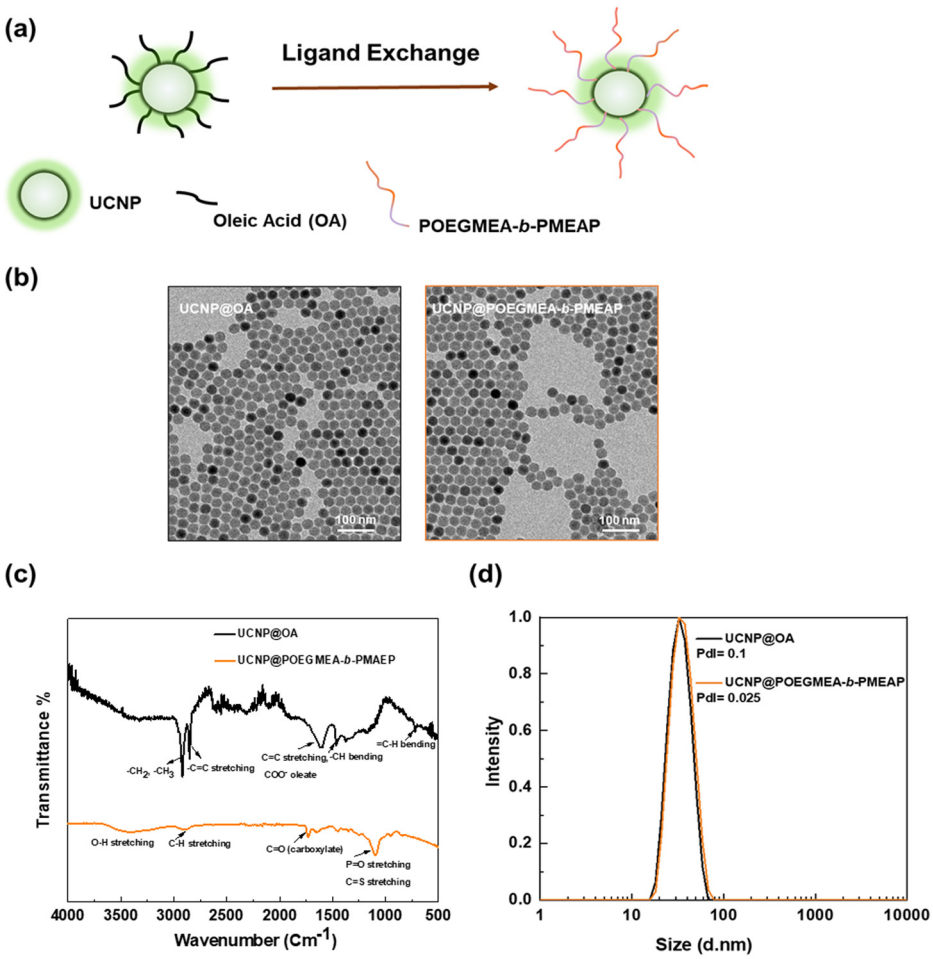

Fig. 1 Characterization of UCNPs. (a) Schematic of the UCNPs functionalization with the polymer (POEGMEA-*b*-PMEAP) *via* ligand exchange. (b) TEM images of UCNP@OA and UCNP@POEGMEA-*b*-PMEAP. (c) FT-IR spectra of UCNPs before and after polymer functionalization. (d) DLS CONTIN plot of UCNP@OA and UCNP@POEGMEA-*b*-PMEAP.

were gated using a 191Ir *versus* event length plot. The mean number of particles per cell was calculated using the 193Ir transmission factor.

Results and discussion

Characterization of the polymer-coated upconversion nanoparticles (UCNP@POEGMEA-*b*-PMAEP)

To prepare the well-dispersed and stable UCNPs in physiological environments, ligand exchange was carried out to replace the oleic acid (OA) on the surface of UCNPs (Fig. 1a). Transmission electron microscopy (TEM) was used to measure the NPs core size, distribution, and morphology before and after coating with polymer. As shown in Fig. 1b, the as-synthesized UCNPs were highly monodispersed before and after modification with polymer, which reveals the homogenous spherical morphology with a core size of 23 ± 0.5 nm. Typical FT-IR peaks at 2917, 2850, 1596, 1465, and 720 cm^{-1} of the UCNP@OA were associated with the symmetric and asymmetric vibrations of the methylene $-CH_2$, C═C, and C═O (oleate) vibration stretches, C–H bending of methylene, and ═C–H bending of double bond (C═C) of the long chain OA ligands, respectively (Fig. 1c). The broad peak at 3411 cm^{-1} is associated with the O–H symmetric stretching bond of the carboxylic acid of the polymer. The peaks at 2917, 1732, and 1101 cm^{-1} are attributed to the stretching vibrations of the $-CH_2-$ and C–C bonds, and the C═O and P═O vibration stretches of the polymer, which confirmed the successful ligand exchange. To further study the performance of the polymer-coated UCNPs, the hydrodynamic size of the NPs was measured by Zetasizer. The DLS CONTIN plot in Fig. 1d shows that the hydrodynamic size (Z-average) of the polymer-coated UCNPs was 32 ± 0.5 with PdI = 0.025, which illustrated that this polymer kept the single UCNPs monodispersed with a narrow size distribution, and UCNPs with this polymer did not show any sign of aggregation. Since the carboxylic acid functional group contained in the polymer will be ionized in aqueous solutions and generate the deprotonated COO–, a negative surface charge (–18 mV ± 0.5) was observed, as shown in Fig. S2.†

Schematic workflow of deep immune profiling

According to our previous research,[35–37] a higher concentration of metal-based NPs signal can saturate the Helios mass cytometry platform. Therefore, a comprehensive assessment of the UCNP@polymer detection limit is necessary before proceeding with these analyses. In order to improve the low concentration limitations, we evaluated the detection limit of UCNP@polymer per cell with a wide concentration range from 5 ppb to 3000 ppb (data is not shown). Based on preliminary data, UCNP@polymer concentrations of 0.5, 1, and 2 ppm were chosen for further experimental analysis. In this study, we performed a dose-dependent exposure of UCNP@polymer to hPBMCs for 3 hours to explore the cellular association and toxicity responses at the single-cell level using high-dimensional mass cytometry. A schematic overview of the mass cytometry analysis performed in this study is shown in Fig. 2.

Furthermore, the heterogeneous immune cell types from hPBMC were identified based on the expression pattern of surface markers (Table 1) with clusters of differentiation (CD). To visualize the immune leukocytes, a manual gating strategy was used (shown in Fig. S1†), to distinguish 12 different immune cell types of hPBMC.

Cell type identification

To visualize the heterogeneous immune cell types population differences, we performed the UMAP computational approach to create the single-cell resolution plot. The manually gated major immune cell types include the naïve/memory B cells (dark gray and yellow colors), plasmacytoid (pDCs)/myeloid (mDCs) dendritic cells (blue and light gray colors), classical/intermediate/non-classical monocytes (pink, purple, and green colors), naïve/memory T helper (CD4+ T cells) cells (dark and light green colors), naïve/memory T killer (CD8+ T cells) cells (orange and red colors), and neutrophils (light blue color), as shown in Fig. 3a. The manually gated unassigned cells were represented by light yellow dots scattered across UMAP. Fig. 3b represents the cell number percentage in the different cell types, which is calculated based on the manual gating results. Among all manually gated immune cell types, phagocytic cells such as mDCs

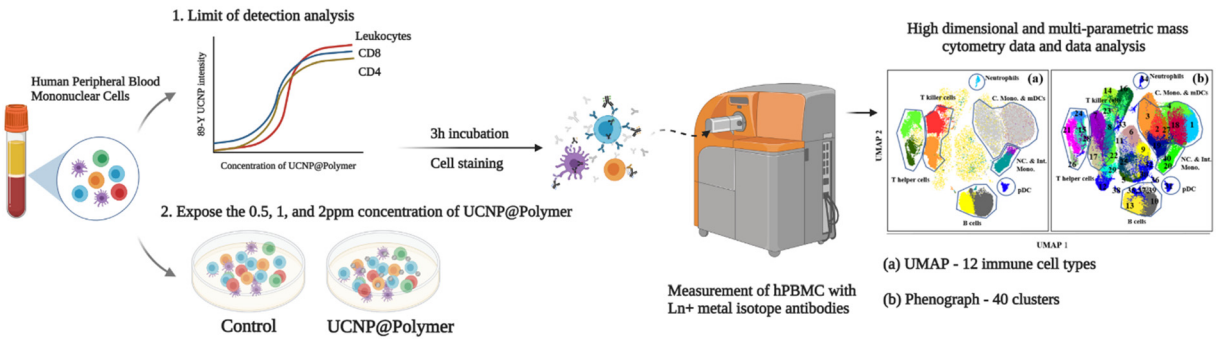

Fig. 2 Schematic representation of the experiment workflow.

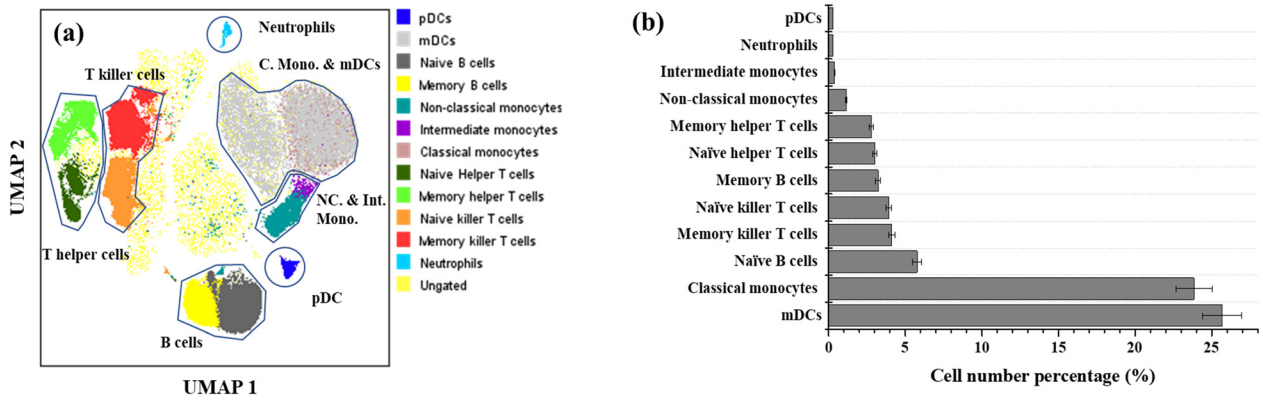

Fig. 3 (a) UMAP plot of the manually gated immune cell types with different colors: pDCs, mDCs, naïve and memory B cells, non-classical monocytes (NC. Mono.), intermediate monocytes (Int. Mono.), classical monocytes (C. Mono.), T killer cells, T helper cell, and neutrophils. (b) Comparison of each immune cell type's abundance, which is the ratio of the cell numbers in each cell type compared to the total number of live cells, averaged across the untreated and UCNP@polymer treated samples.

(25.67%) and classical monocytes (23.84%) were identified as the highest cell number percentage, followed by 5.76% of naïve B cells, 4.1% of memory T killer cells, 3.9% of naïve T killer cells, 3.21% of memory B cells, 3% of naïve T helper cells, 2.8% of memory T helper cells, 1.14% of non-classical monocytes, whereas the intermediate monocytes, neutrophils, and pDCs had the lowest cell number percentages, 0.38%, 0.28% and 0.27%, respectively.

Cell-associated UCNPs and cytotoxicity

Based on the physicochemical and optical properties of UCNPs, they will provide opportunities for biomedical applications with non-toxic, low auto-fluorescence, and improved tissue penetration depth. UCNPs generally exhibit negligible cytotoxicity for their respective biological applications in different cell lines.[38] Recently, Dayong Jin's group reported on PPEGMEMA-*b*-PEGMP$_3$ polymer-coated UCNPs, which have good biocompatibility at high concentration (500 ppm) for MCF-7, MDA-MB-231, and RAW 264.7 cell lines.[39] However, some of the cases reported that apoptosis occurred at a high cellular dose of UCNPs.[15–18] Based on the previous studies,[40–42] UCNPs come into contact with human tissues and cells, which can trigger inflammatory reactions that might cause cellular damage. Therefore, before applying UCNPs to clinical application, interactions between the UCNPs and human immune cells, and their biocompatibility must be studied at the single-cell level with heterogeneous systems.

In this study, we performed cisplatin staining analysis to assess the cytotoxicity and cellular association of UCNPs (in ^{89}Y mean intensities) with hPBMC to explore the heterogeneity at a single-cell level. Furthermore, we used UMAP visualizations of the high-dimensional mass cytometry data to show qualitative analysis of the heterogeneous immune cell types associated with UCNPs (Fig. 4). In the UMAP plots, substantial cellular associations of UCNP@polymer were observed in almost all immune cell types at the 2 ppm level of the UCNP@polymer treated sample, especially for phagocytic cells such as the classical monocytes (C. Mono.), intermediate monocytes (Int. Mono.), non-classical monocytes (NC. Mono.), pDCs, and mDCs (Fig. 4a). Correspondingly, in Fig. 4b, UMAP plots present the cisplatin signal intensity in the control and UCNP@polymer-treated hPBMC groups. Quantitative analysis of the cellular association of UCNPs and cisplatin uptake are illustrated to support the UMAP plots. The data showing the mean intensity of the cell-associated UCNPs in the immune cell types (Fig. 4c) demonstrate the amount of both intracellular and membrane-bound UCNP@polymer, and confirm the observation from the UMAP plots. Similar to previous findings, our results demonstrated that NPs in the human blood are primarily captured by macrophages and monocytes in the circulation and in tissues.[43] This is because they are phagocytic cells, which have a greater tendency to ingest foreign particles compared to other cells, as well as non-phagocytic cells.[44,45] Cisplatin uptake with dose-dependent responses is shown in Fig. 4d. The manually gated immune cell types showed lower cisplatin uptake compared to the untreated sample, except mDCs. Cisplatin is a molecule that can penetrate late apoptotic and necrotic cells that have lost their membrane integrity. The higher cisplatin intensity corresponds to the cell death.[40] In our findings, the cisplatin intensity decreased with increasing concentration of UCNP@polymer in almost all cell types. This indicates that UCNP@polymer is non-toxic and even results in enhanced cell viability. In contrast, mDCs are the only cell type that indicated cell toxicity compared to the untreated sample. It was found to be the immune cell type with the highest cell number percentage, and the statistics are summarized in Table S1.† Therefore, mDCs seem to play key roles in the interactions between immune systems and the UCNPs, for instance, *via* transfer of antigen information to the other cell types, such as T cells and B cells.[46,47] During these interactions, some mDCs (*i.e.*, subsets of mDCs) may strongly interact with the UCNPs, and may result in the higher cytotoxicity observed compared to the other cell types.

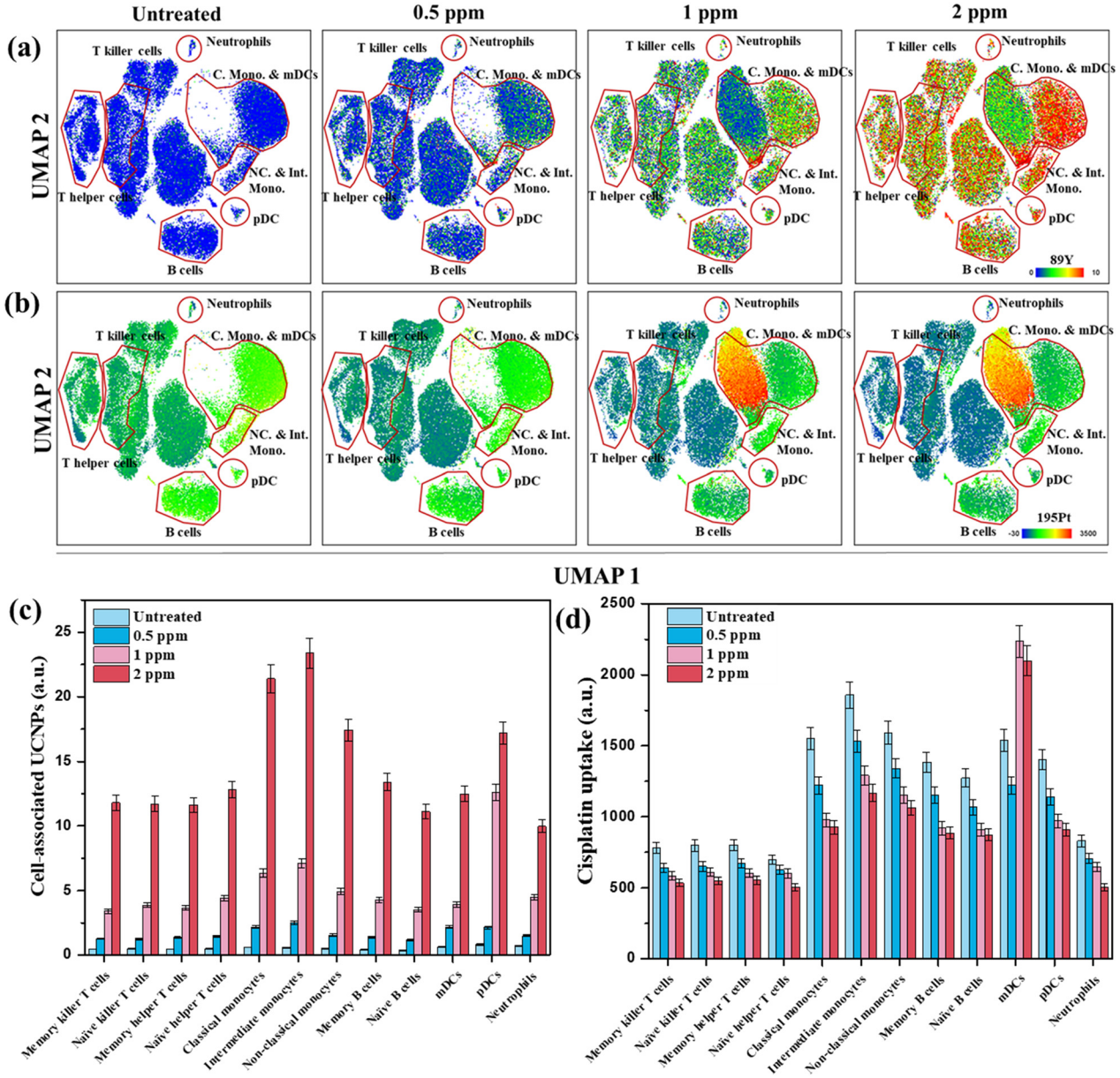

Fig. 4 Comparisons of cell-associated UCNPs and cellular death of the hPBMCs for the untreated and UCNP treated samples, with UMAP plots overlaid with (a) the relative amounts of cell-associated UCNPs and (b) cellular death. Bar-graphs of (c) the relative amounts of cell-associated UCNPs and (d) cellular death, measured *via* ^{89}Y intensity and cisplatin uptake, respectively.

Although mass cytometry is a very powerful single-cell based technique, it cannot distinguish between intracellular and membrane-bound UCNP@polymer. It does have the capability to be completely utilized in nanotoxicological studies.[35–37] Therefore, our main goal here is to highlight the advantages of mass cytometry in nanocomposite toxicology by analysing cell-associated UCNPs in primary human immune cells.

Identification of immune cell subsets populations

In addition to manual gated data analysis, phenograph (PG), an unsupervised automatic clustering algorithm, was applied to discover immune subset types. PG provides a graph-based approach for efficiently locating subpopulations in high-dimensional single-cell mass cytometry data. The PG algorithm identifies clusters of phenotypically similar cells,[48] which is based on the Euclidean distance to define the nearest neighbours for each cell. A total of 40 immune subset types were identified by the PG clustering, as shown in Fig. 5, and most of these clusters were matched to manually gated immune cells (Fig. 3a). The unsupervised PG clustering was identified as subsets; in particular, three subset populations from the classical monocytes (PG#1, 4, 18), four subset clusters of mDCs (PG#2, 3, 19, 27) and naïve B cells (PG#10, 35, 37, 39), two subset clusters of memory T killer cells

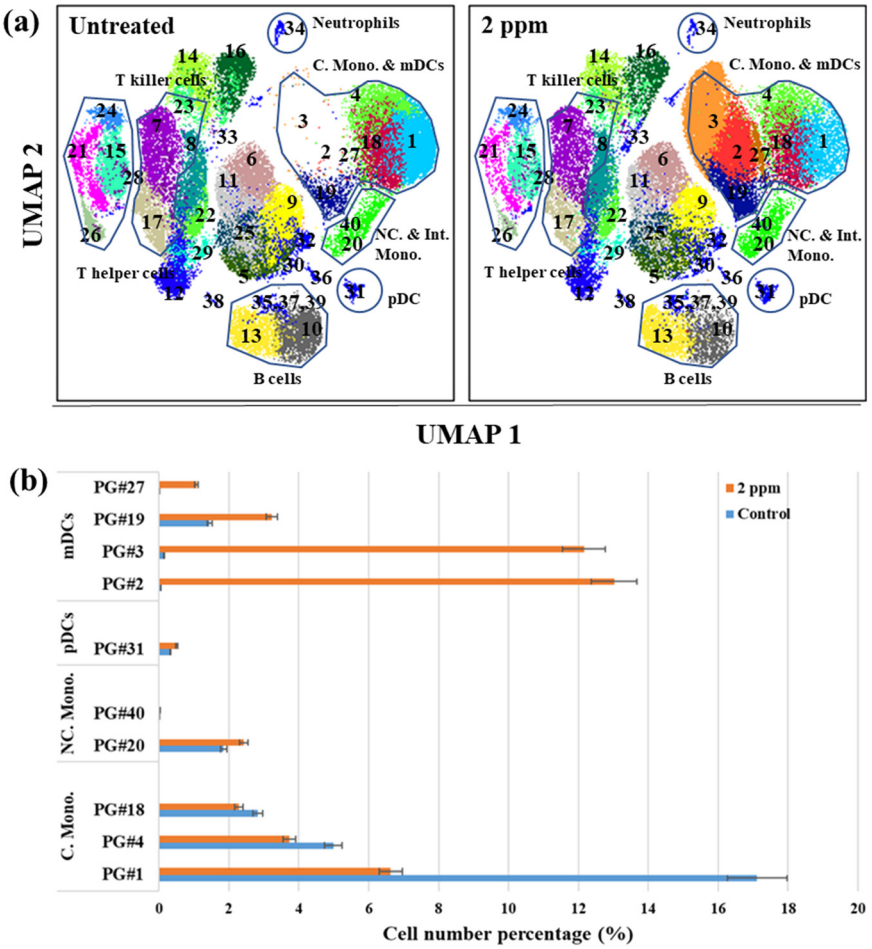

Fig. 5 Population abundance of the phenograph clusters of immune cells. (a) Phenograph clusters overlaid on the UMAP of untreated and 2 ppm samples. (b) Bar graph of the significant cell types related to the UCNP toxicity: mDCs, pDCs, non-classical monocytes (NC. Mono.), and classical monocytes (C. Mono.).

(PG#7, 23), and non-classical monocytes (PG#20, 40). The other cell types, such as pDCs (PG#31), memory B cells (PG#13), naïve T helper cells (PG#26), memory T helper cells (PG#24), naïve T killer cells (PG#17), and neutrophils (PG#34) were clustered as one type, and all of the statistics of PG clustering is summarized in Table S2.†

Based on Fig. 4, we found that monocytes and mDCs had significant differences in the treated samples. In particular, for the 2 ppm UCNP@polymer-treated sample, the mDCs cell number percentage increased, whereas the cisplatin signal also increased. Interestingly, from the PG clustering algorithm, we identified sub-cell types of mDCs, which are PG#2, PG#3, PG#19, and PG#27, and a high cell number percentage in the 2 ppm UCNP@polymer-treated sample. The pDCs and NC. Mono. were revealed to be similar to the mDCs sub-cell types. In contrast, the sub-cell types of C. Mono., which include the PG#1, PG#4, and PG#18 clusters, were identified to have higher cell number percentages in the

Table 2 List of cellular phenotypic surface markers expression

Cell types	Phenograph clusters	Marker expression
pDCs (1)	#31	$CD123^{mid}HLA\text{-}DR^{mid}CD45RA^{mid}$
mDCs (4)	#2	$CD123^{low}HLA\text{-}DR^{low}CD11c^{mid}CD45RA^{low}$
	#3	$CD123^{low}HLA\text{-}DR^{low}CD11c^{mid}CD45RA^{low}$
	#19	$CD123^{low}HLA\text{-}DR^{mid}CD11c^{mid}CD45RA^{low}$
	#27	$CD123^{low}HLA\text{-}DR^{mid}CD11c^{mid}CD45RA^{low}$
Non-classical monocytes (2)	#20	$CD14^{low}CD16^{mid}HLA\text{-}DR^{mid}CD11c^{mid}CD45RA^{mid}$
	#40	$CD14^{low}CD16^{low}HLA\text{-}DR^{mid}CD11c^{mid}CD45RA^{low}$
Classical monocytes (3)	#1	$CD14^{low}CD16^{low}HLA\text{-}DR^{low}CD11c^{mid}CD45RA^{mid}$
	#4	$CD14^{mid}CD16^{low}HLA\text{-}DR^{mid}CD11c^{mid}CD45RA^{low}$
	#18	$CD14^{mid}CD16^{low}HLA\text{-}DR^{high}CD11c^{low}CD45RA^{low}$

control sample compared to the treated samples, as shown in Fig. 5b.

Fig. S3† demonstrates a significant difference of the surface marker expression, where PG#2, PG#3, PG#19, and PG#27 were predominant in the UCNP@polymer treated samples. In Table 2, PG#31 is related to pDCs expressing $CD123^{mid}HLA\text{-}DR^{mid}CD45RA^{mid}$. Interestingly, the PG#2 and #3 clusters show similar marker expressions as $CD123^{low}$-$HLA\text{-}DR^{low}CD11c^{mid}CD45RA^{low}$, whereas PG#19 and #27 show the same marker expressions as $CD123^{low}HLA\text{-}DR^{mid}$-$CD11c^{mid}CD45RA^{low}$. In the case of the monocytes, the PG#20 cluster expressed $CD14^{low}CD16^{mid}HLA\text{-}DR^{mid}CD11c^{mid}$-$CD45RA^{mid}$, while the PG#40 clusters expressed $CD14^{low}$-$CD16^{low}HLA\text{-}DR^{mid}CD11c^{mid}CD45RA^{low}$. The identified sub-cell types of C. Mono., PG#1 cluster $CD14^{low}CD16^{low}HLA$-$DR^{low}CD11c^{mid}CD45RA^{mid}$, PG#4 cluster $CD14^{mid}CD16^{low}$-$HLA\text{-}DR^{mid}CD11c^{mid}CD45RA^{low}$, and PG#18 cluster $CD14^{mid}$-$CD16^{low}HLA\text{-}DR^{high}CD11c^{low}CD45RA^{low}$ were differently expressed. We investigated the surface marker intensity difference between the control and 2 ppm UCNP@polymer treated samples.

The current understanding of the NP cellular association is as follows. Since monocytes and DCs are important antigen-presenting cells (APCs), they have a natural tendency to ingest foreign particles *via* phagocytosis.[45,49] According to previous studies,[47,50] APCs identify NPs as foreign antigens, engulf and digest them, and then deliver them to other cells *via* the major histocompatibility complex (MHC), priming the antigen-specific cellular immune response. The POEGMEA-*b*-PMAEP polymer-coated UCNPs were preferentially associated with APCs, such as monocytes ($CD14^{mid}CD16^{low}HLA\text{-}DR^{mid}$-$CD11c^{mid}$) and DCs ($CD123^{low}HLA\text{-}DR^{mid}CD11c^{mid}$-$CD45RA^{low}$), to initiate immune responses.

Conclusions

In summary, we have used single-cell mass cytometry to investigate the cellular association and toxicity of the POEGMEA-*b*-PMAEP polymer-coated $NaYF_4$:Yb^{3+}/Er^{3+} UCNPs in hPBMCs. The 12 immune cell types were identified, and we observed the heterogeneous interactions between different cell types and the UCNP@polymer with various concentrations (*i.e.*, at 0.5–2 ppm administered doses, for 3 h exposure time). The elemental detection capability of mass cytometry enabled us to measure the cell-associated UCNPs and nanotoxicity based on the cisplatin signal. Therefore, we found that phagocytic cells (such as monocytes and dendritic cells) had higher affinity to the UCNPs than the other non-phagocytic cells. In addition, PG clustering algorithms were used to identify sub-cell types of monocytes and dendritic cells, which is sub-divided into 3 clusters (PG#1, 4, 18) and 4 clusters (PG#2, 3, 19, 27), respectively. Our study demonstrated a new technical framework to understand the heterogeneous interactions of conventional nanomaterials with complex human immune cells, which will be helpful for the safe use of nanomaterials in biomedical applications.

Author contributions

T. H. Y. designed and conceptualized the experiment, Z. G. designed and carried out most of the experimental studies, and wrote the original manuscript draft, H. P. and M. M. reviewed and edited the manuscript and revisions. M. M. and D. Y. J. carried out the synthesis of the nanoparticles and performed their characterization. J. S. carried out isolation of hPBMC and reviewed manuscript. All authors read and approved the final manuscript.

Conflicts of interest

There are no conflicts to declare.

Acknowledgements

This work was supported by the Nano Material Technology Development Program, grant no. 2021M3A7B6031397, and the Basic Science Research Program, grant no. 2020R1A6A1A06046728, of the National Research Foundation of Korea funded by the Ministry of Science, ICT, and the Ministry of Education.

Notes and references

1 M. Dessale, G. Mengistu and H. M. Mengist, *Int. J. Nanomed.*, 2022, **17**, 3735–3749.
2 H. M. Abdel-Mageed, N. Z. AbuelEzz, R. A. Radwan and S. A. Mohamed, *J. Microencapsulation*, 2021, **38**, 414–436.
3 Z. Gerelkhuu, B. T. Huy, M. Sharipov, D. Jung, T.-L. Phan, E. D. Conte and Y.-I. Lee, *Mater. Sci. Eng., C*, 2018, **86**, 56–61.
4 Z. Gerelkhuu, D. Jung, B. The Huy, S. M. Tawfik, M. L. Conte, E. D. Conte and Y.-I. Lee, *Sens. Actuators, B*, 2019, **284**, 172–178.
5 Z. Gerelkhuu, B. T. Huy, J. W. Chung and Y.-I. Lee, *Bull. Korean Chem. Soc.*, 2015, **36**, 1307–1308.
6 T. X. Trinh, S. J. Kwon, Z. Gerelkhuu, J. S. Choi, J. Song and T. H. Yoon, *J. Synchrotron Radiat.*, 2020, **27**, 720–724.
7 J. W. Chung, Z. Gerelkhuu, J. H. Oh and Y.-I. Lee, *Appl. Spectrosc. Rev.*, 2016, **51**, 678–705.
8 W. Li, G. Zhang and L. Liu, *Front. Bioeng. Biotechnol.*, 2021, **9**, 768927.
9 S. Sargazi, I. Fatima, M. Hassan Kiani, V. Mohammadzadeh, R. Arshad, M. Bilal, A. Rahdar, A. M. Díez-Pascual and R. Behzadmehr, *Int. J. Biol. Macromol.*, 2022, **206**, 115–147.
10 J. Liu, R. Li and B. Yang, *ACS Cent. Sci.*, 2020, **6**, 2179–2195.
11 M. R. Younis, G. He, J. Qu, J. Lin, P. Huang and X.-H. Xia, *Adv. Sci.*, 2021, **8**, 2102587.
12 D. Xiao, H. Qi, Y. Teng, D. Pierre, P. T. Kutoka and D. Liu, *Nanoscale Res. Lett.*, 2021, **16**, 167.
13 A. Rajaee, S. Wang, L. Zhao, D. Wang, Y. Liu, J. Wang and K. Ying, *Phys. Med. Biol.*, 2019, **64**, 195007.
14 A. Jakhmola, N. Anton and T. F. Vandamme, *Adv. Healthcare Mater.*, 2012, **1**, 413–431.

15 A. Detappe, E. Thomas, M. W. Tibbitt, S. Kunjachan, O. Zavidij, N. Parnandi, E. Reznichenko, F. Lux, O. Tillement and R. Berbeco, *Nano Lett.*, 2017, **17**, 1733–1740.
16 M.-A. Shahbazi, L. Faghfouri, M. P. A. Ferreira, P. Figueiredo, H. Maleki, F. Sefat, J. Hirvonen and H. A. Santos, *Chem. Soc. Rev.*, 2020, **49**, 1253–1321.
17 S. Wen, J. Zhou, K. Zheng, A. Bednarkiewicz, X. Liu and D. Jin, *Nat. Commun.*, 2018, **9**, 2415.
18 M. Patel, M. Meenu, J. K. Pandey, P. Kumar and R. Patel, *J. Rare Earths*, 2022, **40**, 847–861.
19 S. Yamini, M. Gunaseelan, A. Gangadharan, S. A. Lopez, K. S. Martirosyan, A. Girigoswami, B. Roy, J. Manonmani and S. Jayaraman, *Nanotechnology*, 2021, **33**, 85202.
20 L. Zhang, D. Jin and M. H. Stenzel, *Biomacromolecules*, 2021, **22**, 3168–3201.
21 A.-R. Hong, J.-H. Kyhm, G. Kang and H. S. Jang, *Nano Lett.*, 2021, **21**, 4838–4844.
22 A. Ghazy, M. Safdar, M. Lastusaari, H. Savin and M. Karppinen, *Sol. Energy Mater. Sol. Cells*, 2021, **230**, 111234.
23 C. Liu, X. Zheng, T. Dai, H. Wang, X. Chen, B. Chen, T. Sun, F. Wang, S. Chu and J. Rao, *Angew. Chem., Int. Ed.*, 2022, **61**, e202116802.
24 H. Oliveira, A. Bednarkiewicz, A. Falk, E. Fröhlich, D. Lisjak, A. Prina-Mello, S. Resch, C. Schimpel, I. V. Vrček, E. Wysokińska and H. H. Gorris, *Adv. Healthcare Mater.*, 2019, **8**, 1801233.
25 G. Tian, L. Duan, X. Zhang, W. Yin, L. Yan, L. Zhou, X. Liu, X. Zheng, J. Li, Z. Gu and Y. Zhao, *Chem. – Asian J.*, 2014, **9**, 1655–1662.
26 R. Li, Z. Ji, J. Dong, C. H. Chang, X. Wang, B. Sun, M. Wang, Y.-P. Liao, J. I. Zink, A. E. Nel and T. Xia, *ACS Nano*, 2015, **9**, 3293–3306.
27 M. Alkahtani, N. Alsofyani, A. Alfahd, A. A. Almuqhim, F. A. Almughem, A. A. Alshehri, H. Qasem and P. R. Hemmer, *Nanomaterials*, 2021, **11**, 284.
28 M. Alkahtani, A. Alfahd, N. Alsofyani, A. A. Almuqhim, H. Qassem, A. A. Alshehri, F. A. Almughem and P. Hemmer, *Nanomaterials*, 2021, **11**, 1535.
29 P. P. Nampi, A. Vakurov, L. E. Mackenzie, N. S. Scrutton, P. A. Millner, G. Jose and S. Saha, *J. Biophotonics*, 2019, **12**, e201800256.
30 A. Adan, G. Alizada, Y. Kiraz, Y. Baran and A. Nalbant, *Crit. Rev. Biotechnol.*, 2017, **37**, 163–176.
31 J. Liu, Z. Liu, Y. Pang and H. Zhou, *J. Nanobiotechnol.*, 2022, **20**, 127.
32 B. Fadeel, *Front. Immunol.*, 2019, **10**(133), 1–10.
33 M. Maddahfar, S. Wen, S. M. Hosseinpour Mashkani, L. Zhang, O. Shimoni, M. Stenzel, J. Zhou, B. Fazekas de St Groth and D. Jin, *Bioconjugate Chem.*, 2021, **32**, 1146–1155.
34 H. T. T. Duong, Y. Chen, S. A. Tawfik, S. Wen, M. Parviz, O. Shimoni and D. Jin, *RSC Adv.*, 2018, **8**, 4842–4849.
35 M. K. Ha, S. J. Kwon, J.-S. Choi, N. T. Nguyen, J. Song, Y. Lee, Y.-E. Kim, I. Shin, J.-W. Nam and T. H. Yoon, *Small*, 2020, **16**, 1907674.
36 J. Bae, M. Ha, H. Perumalsamy, Y. Lee, J. Song and T.-H. Yoon, *Pharmaceutics*, 2022, **14**(3), 630.
37 M. K. Ha, J.-S. Choi, S. J. Kwon, J. Song, Y. Lee, Y.-E. Kim and T. H. Yoon, *Environ. Sci.: Nano*, 2020, **7**, 1102–1114.
38 H. Dong, S.-R. Du, X.-Y. Zheng, G.-M. Lyu, L.-D. Sun, L.-D. Li, P.-Z. Zhang, C. Zhang and C.-H. Yan, *Chem. Rev.*, 2015, **115**, 10725–10815.
39 L. Zhang, C. Chen, S. S. Tay, S. Wen, C. Cao, M. Biro, D. Jin and M. H. Stenzel, *ACS Appl. Mater. Interfaces*, 2021, **13**, 16142–16154.
40 H. G. Fienberg, E. F. Simonds, W. J. Fantl, G. P. Nolan and B. Bodenmiller, *Cytometry, Part A*, 2012, **81**, 467–475.
41 Y. Chen, O. Shimoni, G. Huang, S. Wen, J. Liao, H. T. T. Duong, M. Maddahfar, Q. P. Su, D. G. Ortega, Y. Lu, D. H. Campbell, B. J. Walsh and D. Jin, *Cytometry, Part A*, 2022, **101**, 400–410.
42 G. Huang, Y. Zhu, S. Wen, H. Mei, Y. Liu, D. Wang, M. Maddahfar, Q. P. Su, G. Lin, Y. Chen and D. Jin, *Nano Lett.*, 2022, **22**, 3761–3769.
43 J. Jia, Y. Zhang, Y. Xin, C. Jiang, B. Yan and S. Zhai, *Front. Oncol.*, 2018, **8**, 404.
44 B. S. Zolnik, A. González-Fernández, N. Sadrieh and M. A. Dobrovolskaia, *Endocrinology*, 2010, **151**, 458–465.
45 Y.-H. Luo, L. W. Chang and P. Lin, *BioMed Res. Int.*, 2015, **2015**, 143720.
46 A. Cifuentes-Rius, A. Desai, D. Yuen, A. P. R. Johnston, N. H. Voelcker, A. J. Grippin, B. Wummer, T. Wildes, K. Dyson, V. Trivedi, C. Yang, M. Sebastian, H. R. Mendez-Gomez, S. Padala, M. Grubb, M. Fillingim, A. Monsalve, E. J. Sayour, J. Dobson and D. A. Mitchell, *ACS Nano*, 2019, **13**, 13884–13898.
47 A. Cifuentes-Rius, A. Desai, D. Yuen, A. P. R. Johnston and N. H. Voelcker, *Nat. Nanotechnol.*, 2021, **16**, 37–46.
48 J. H. Levine, E. F. Simonds, S. C. Bendall, K. L. Davis, E. D. Amir, M. D. Tadmor, O. Litvin, H. G. Fienberg, A. Jager, E. R. Zunder, R. Finck, A. L. Gedman, I. Radtke, J. R. Downing, D. Pe'er and G. P. Nolan, *Cell*, 2015, **162**, 184–197.
49 B. S. Zolnik, A. González-Fernández, N. Sadrieh and M. A. Dobrovolskaia, *Endocrinology*, 2010, **151**, 458–465.
50 M. Y. Gerner, P. Torabi-Parizi and R. N. Germain, *Immunity*, 2015, **42**, 172–185.